New developments in ground probing radar: the possibility of reconstructing a holographic image of underground reflectivity

Luigi Giubbolini ([1]) **and Luigi Sambuelli** ([2])

([1]) *IRITI, CNR, c/o Politecnico di Torino, Italy*

([2]) *Dipartimento di Georisorse e Territorio, Politecnico di Torino, Italy*

Abstract

During the last decade GPR has developed rapidly: instruments have become more compact and more digital, the field of application has broadened from non-destructive testing to humanitarian demining. Studies have been carried out to analyse the full information content of the backscattered wavefield trying to go beyond the time and amplitude analysis. In recent years, many researchers have focused on the possibility of applying holographic acquisition and processing to GPR data. This paper proposes a theoretical outline of a holographic acquisition and processing techniques; a block diagram of the proposed holographic radar; the outlines of the design and the realisation of a custom-built full-scale test-site and the results of the first simulations carried out with newly developed software. The basic rules for an optimum choice of the main acquisition parameters are also given together with a discussion of the main advantages and disadvantages of the proposed techniques.

Key words *GPR – radar imaging – polarisation – holography – SAR*

1. Introduction

The use of GPR, from the earliest experiments in glaciology dating back to the sixties, has grown constantly and suddenly boosted from about 1970 when the first portable equipment, using improvements developed during GPR use in Vietnam war, became available. The acronym GPR is often referred to as meaning Ground Penetrating Radar, less frequently Ground Prob-ing Radar, sometimes Ground Pulsed Radar. The latter best represents the electromagnetic principle on which GPR is based. The first use of pulsed radar to investigate subsoil dates back to a German patent of Hülsenbeck in 1926.

Pulsed GPR is today the most commonly used system in geophysical and environmental applications. It detects the amplitude of reflect-ed signals in the time domain and achieves high spatial resolution by means of the coherent data processing of signals backscattered by buried targets or by stratigraphical and geological interfaces.

In pulsed GPR, the phase of the signal is not acquired so that at least half of the travelling information is missed and a lack of resolution results during image elaboration of the target.

Today there exists much literature on pulsed GPR (Ulriksen, 1982; Daniels *et al.*, 1988) and

on many of its peculiar applications: soil stratig-raphy determination (Davis and Annan, 1989); archaeological and engineering uses (Goodman, 1994; Sambuelli *et al.*, 1998); underground struc-tures detection and diagnosis (Bae *et al.*, 1996). Even in the environmental field, GPR provides good results in the detection of buried waste containers.

Many attempts have also been made to de-tect hydrocarbon contaminants, such as immis-cible oil (NAPL – Non-Aqueous Phase Liquids) in soils and groundwater (Daniels *et al.*, 1992; Guo *et al.*, 1997).

Instead of the faster, traditional, near-zero-offset singlefold techniques, an improvement in radar results can be achieved by employing multifold data acquisition which enhances the signal to noise ratio (Pipan *et al.*, 1996). This technique, borrowed from reflection seismic, requires greater complexity in data acquisition and processing. However, since the electromag-netic properties of the soils differ from seismic properties and loss characteristics of the medi-um can heavily influence the signals, a straight-forward application of seismic processing can yield misleading results (Van Deen, 1996).

One of the major shortcomings of tradition-al radar equipment is the low readability by the end users of resulting images. The true shape of a detected object, in a «space *versus* round-trip-time» section, is very often reduced to a more or less smooth and faint rounded area. Neither can specialised processing go much deeper into the object shape definition whenever this shape becomes a little more complicated and sharp. The evidence of sharp corners is almost absent and their presence is recognised very often only by an *a priori* knowledge of the target shape.

A further step in the direction of a more readable form of radar result could then be ob-tained using polarisation properties of sharp edges (like corners) with respect to the reflec-tion of an electromagnetic field impinging on it. This improvement can be achieved provided that both transmitting and receiving antennas are made by two orthogonal dipoles. In such a way four images are acquired on the same pro-file: HH, HV, VH, VV. It can easily be shown that the comparison of these results can enhance

the presence of sharp edges, mainly if they are parallel to one of the dipole directions (Miwa *et al.*, 1996).

Moreover, polarimetric filtering can also be applied in order to enhance the visibility of a target with respect to cluttering (Yamaguchi *et al.*, 1996.). Acquisition of the aforementioned four components constitutes the elements of the polarimetric scattering characterisation in an HV polarisation basis. The possibility to obtain the reflectivity matrix of the subsoil, and of a spec-ified target, can also be helpful in determination of the material constituting the target itself.

As far as the resolution is concerned, it can be shown that, with respect to pulsed radar, an increase resolution can be obtained with a Syn-thetic Aperture Radar (SAR) acquisition. More-over, if a Frequency Modulated Continuous Wave (FMCW) is used, not only the resolution but also the target shape definition can be fur-ther enhanced (Al-Ghamdi and Afifi, 1996). It has also been recognised that interferometry and holographic data processing of FMCW ra-dar data can improve resolution and S/N ratio (Al-Ghamdi and Afifi, 1996; Leuschen *et al.*, 1996).

The development of holography in earth sci-ence applications started at the end of the seven-ties. A single fixed frequency in Continuous Wave modality (CW) was first used to verify the reliability in the image reconstruction of objects buried at a depth of a few centimetres. Refine-ment of the technique allowed some experi-ments to be carried out to evaluate the capability of detecting buried targets in ice and snow. A high resolution was achieved using a frequency range of 8 and 10 GHz (Sakamoto and Aoki, 1985).

Some preliminary tests were carried out us-ing a fixed antenna and a mobile scenario; these experiments, performed in the IRITI laboratory, aimed to check the reliability of 3D imaging of the holographic technique in the microwave fre-quency band (Giubbolini, 1999).

2. The holographic signal

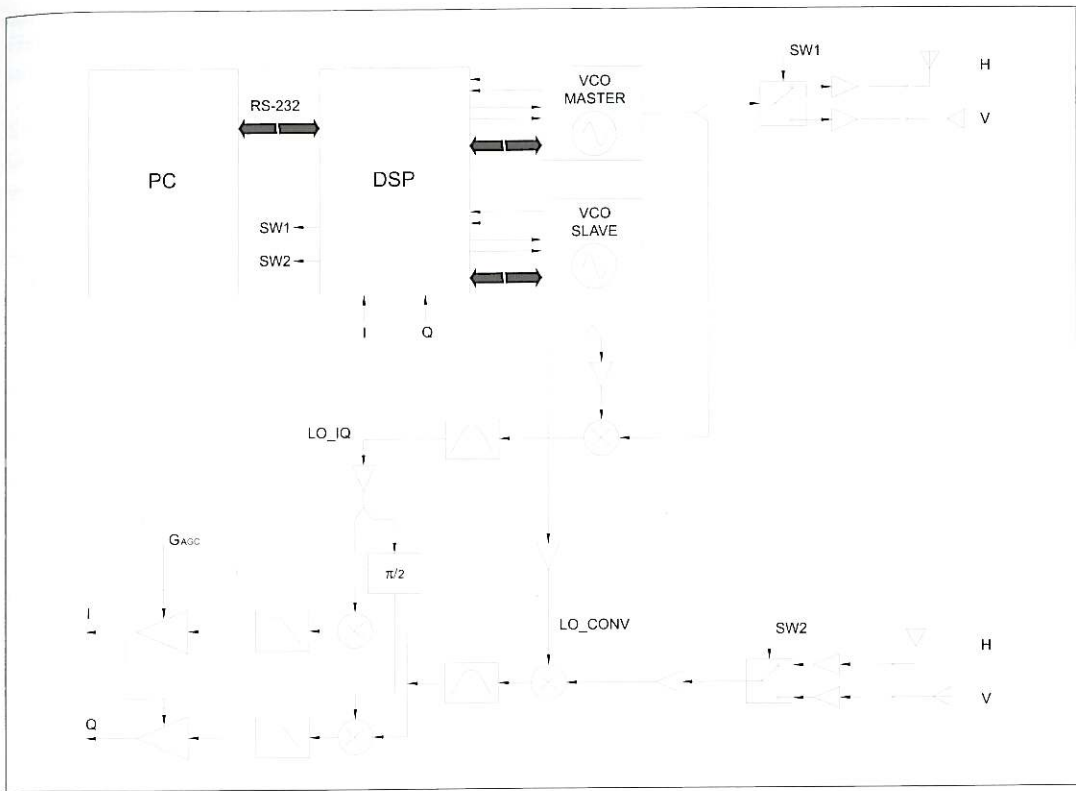The block diagram in fig. 1 proposes a Stepped-Frequency Modulated Wave bi-static

Fig. 1. HGPR architecture.

Radar which main parameters are shown in table I. It has one transmitter and one receiver working with continuous wave signal whose frequency is increased following a step-modulation scheme. The antennas have wide beamwidth ($\pm 90°$ in azimuth as well as in elevation) in order to cover the largest part of the volume to be imaged and wide bandwidth (0.4-0.8 GHz) to obtain high resolution. The system is moved in different positions and acquires the *complex reflectivity coefficient* of the subsoil.

In order to acquire the four polarimetric three-dimensional images of the subsoil, the transmitting and receiving antennas can radiate along two linear and orthogonal polarisations, that are the horizontal and vertical polarisations. The two switches (SW1 and SW2) select which polarisation is transmitted and which is received.

The transmitted signal is supplied by the signal generator VCO Master and then radiated by the selected transmitted antenna.

The diffracted wave front from the subsoil is detected from the selected receiving antenna and it is down-converted by mixing it with the Local Oscillator signal (LO_CONV) so that the Intermediate Frequency signal (IF signal) is produced. The LO_CONV signal is given by a second signal generator (the VCO Slave in fig. 1) and its frequency is fixed at 70 MHz from the transmitted frequency. In such a way, the frequency of the IF signal (after pass-band filtering) is 70 MHz irrespective of the transmitted frequency. This scheme permits use of a high performance I-Q demodulator reducing crosstalk and inter-modulation effects, obtaining low amplitude distortion and phase imbalance on

Table I. HGPR parameters.

HGPR parameter	Symbol	Value
Minimum carrier frequency	f_0	0.4 GHz
Radio frequency bandwidth	B_{RF}	400 MHz
Transmitted power	P_T	100 mW
Receiver noise figure	F	3.5 dB
Modulation period range	T_M	1 ÷ 1000 ms
Minimum time sampling	Δt	1 μs
No. of acquired samples	N_r	128 ÷ 1024
Intermediate frequency	f_{IF}	70 MHz
Tx antennas: V-beam width	$\vartheta_{MAX} - \vartheta_{min}$	90°
Tx antennas: H-beam width	$\varphi_{MAX} - \varphi_{min}$	90°
Rx antennas: V-beam width	–	90°
Rx antennas: H-beam width	–	90°
Tx antennas sides: x, z	L_x, L_z	48 cm, 48 cm
Rx antennas sides: x, z	l_x, l_z	48 cm, 48 cm

the In-phase (I) and the in-Quadrature (Q) signals.

The complex signal I + jQ obtained is the complex reflectivity coefficient of the observed scenery from the position of the antennas, that is the interference figure between the radiated and the back-scattered wave.

The collection of this coefficient on a grid of points (scanned area) yields the *holographic interference pattern* (UHF Hologram) for the used polarisation (transmitting and receiving). The four 3D polarimetric images of the observed scenery are obtained from the four holograms through a reconstruction process.

The carrier frequency and the bandwidth are chosen taking into account the application; in fact, in order to be able to detect pollutants down-to 10 m in the subsoil the losses of the ground with frequency bounds the operative frequency up to about 800 MHz. Moreover, a trade-off between the acceptable maximum size of the antenna and bandwidth (that is pro-portional to the radial resolution) bounds the lower frequency down to 400 MHz. With these figures, the size of the antennas could be about 0.5×0.5×0.5 m each and the radial resolution in sand would be about 0.18 m.

The investigated volume is in the near-field of the antenna. Furthermore, scanning the subsoil on a wide ground area, the subsoil volume is investigated from different aspect angles and the buried objects are observed from different sides. For this reason, the set of collected reflectivity coefficients is called Hologram in the UHF band analogously to optical holograms where the holograms are acquired at a single frequency.

The sides of the scanned area are large in terms of wavelengths and similar to the maximum depth. Under these conditions, a scattering point in the subsoil produces a spherical wave-front in the scanned area and in order to reconstruct the three-dimensional image, the focusing process must take into account the exact

solution of the Maxwell equations, that is the Green function, so that the scenery is correctly imaged in the far as well as in the near field.

The transmitted signal is realised with a Stepped-Frequency Continuous Wave modulation of length T_M, with constant frequency step of B_{RF}/N_M

$$S_T(t) = \text{rect}\left(\frac{t}{T_M}\right)\cos\left[2\pi\left(\int_t\left[f_0 + B_{RF}\cdot\right.\right.\right.$$

$$\tag{2.1}$$

$$\left.\left.\left.\cdot\,\text{stair}\left(\frac{t}{T_M}\right)\right]dt\right)\right] = \text{rect}\left(\frac{t}{T_M}\right)\cos[\Phi_T(t)]$$

where: f_0 is the first-step frequency of the modulation function; B_{RF} is the radio frequency bandwidth; $\text{stair}\left(\dfrac{t}{T_M}\right)$ is the stair modulation function of N_M steps and duration T_M that is

$$\frac{\text{int}\left(\dfrac{t}{T_M/N_M}\right)}{N_M}$$

for $t = 0 \ldots T_M$; the function $\text{rect}\left(\dfrac{t}{T_M}\right)$ defines the duration of the radiated wave, and is 0 for $|t| > \dfrac{T_M}{2}$ and 1 for $|t| \leq \dfrac{T_M}{2}$.

The transmitted signal can be radiated along the Vertical (V) polarisation as well as the Horizontal one (H). By means of two modulation periods, both polarisations are transmitted at different times. Let $\bar{r}$ be the vector identifying a generic subsoil point in the spherical co-ordinate system (r, ϑ, φ) the transmitted electrical field is given by

$$\bar{E}_T^i(\bar{r}, \bar{r}_T, t) =$$

$$\tag{2.2}$$

$$= \sqrt{\frac{P_T Z}{4\pi}}\, G_T^i(\vartheta, \varphi)\frac{1}{|\bar{r} - \bar{r}_T|}S_T\left[t - \frac{|\bar{r} - \bar{r}_T|}{v}\right]\hat{p}_T^i$$

where P_T is the transmitted power, Z is the wave impedance of the soil, $\hat{p}_T^i$ is the polarisation unit vector of the transmitting antenna, G_T^i are the radiation diagrams of the transmitting antenna related to the two polarisation $(i = H, V)$, v is the wave velocity in the medium and $\bar{r}_T$ is the location of the transmitter.

Let $\underline{R}(\bar{r})$ be the complex *polarimetric 3D reflectivity matrix* of the investigated volume

$$\underline{R}(\bar{r}) = \begin{bmatrix} R^{HH}(\bar{r}) & R^{VH}(\bar{r}) \\ R^{VH}(\bar{r}) & R^{VV}(\bar{r}) \end{bmatrix} \tag{2.3}$$

the diffracted electric field received at $\bar{r}_R = \bar{r}_T + \bar{r}_{TR}$, where $\bar{r}_{TR}$ is the fix distance between transmitting and receiving antennas along the two polarisation axis, is given by the interference of all the returning echoes

$$\bar{E}_R^{Hi,Vi}(\bar{r}_T, t) =$$

$$\tag{2.4}$$

$$= \int_{\bar{r}}\sqrt{\frac{P_T Z G_T^i(\vartheta, \varphi)}{(4\pi)^2}}\,\frac{\underline{R}(\bar{r})\cdot\hat{p}_T^i}{r_R\cdot r_T}\,S_T\left(t - \frac{r_{RT}}{v}\right)d\bar{r},$$

where:

$$r_{RT} = |\bar{r} - \bar{r}_T| + |\bar{r} - \bar{r}_R| = |\bar{r} - \bar{r}_R - \bar{r}_{TR}| + |\bar{r} - \bar{r}_R| =$$

$$= \sqrt{(x - x_R - x_{TR})^2 + y^2 + (z - z_R)^2} + \tag{2.5}$$

$$+ \sqrt{(x - x_R)^2 + y^2 + (z - z_R)^2}$$

is the *round trip distance* between the transmitting antenna, the scattering centre and the receiving antenna. The *round trip distance* is expressed in Cartesian co-ordinates where y is the depth axis and we have assumed the transmitting and receiving antennas embedded in the same box so that the transmitting antenna is located at: $\bar{r}_T = \bar{r}_R + \bar{r}_{TR} = \bar{r}_R + x_{TR}\cdot\hat{x} = (x_R + x_{TR})\cdot\hat{x} + z_R\cdot\hat{z}$.

The radiation diagrams of the transmitting and receiving antennas (G_T^i, G_R^i) filter the re-

ceived signal in relation to the aspect angle. Supposing that the antennas do not depolarised the wave, that is they have a high polarisation efficiency, and they have the same response in the two polarisations ($G_T^H = G_T^V = G_T$, $G_R^H = G_R^V = G_R$), the received signal from the antenna located at $\bar{r}_R$ is

$$S_R^{j,i}(\bar{r}_R, t) \cong \lambda_0 \sqrt{\frac{P_T Z}{(4\pi)^3}} \ \text{rect}\left(\frac{t}{T_M}\right) \cdot$$

$$\cdot \int_{\bar{r}} \sqrt{G_T \cdot G_R} \ \frac{R^{j,i}(\bar{r})}{r^2} \cos\left\{\Phi_T(t) - \quad (2.6)\right.$$

$$\left. - 2\pi\left[\frac{1}{\lambda_0} + \frac{1}{2\Delta r} \text{stair}\left(\frac{t}{T_M}\right)\right]r_{RT}\right\} d\bar{r}$$

where $(j, i) = (H, V)$; λ_0 is the wavelength of the electromagnetic wave in the medium at the minimum frequency; $\Delta r = v/(2 \cdot B_{RF})$ is the range resolution in the medium; $S_R^{j,i}$ refers to the four modulating periods.

In eq. (2.6) the apex i identifies the polarisation of the transmitted wave and j the polarisation of the selected receiving antenna. Transmitting two signals with horizontal and two signals with vertical polarisations during four successive modulation periods, and acquiring the horizontal and vertical components of the received wave, it is possible to collect four received signals related to the four components of the reflectivity matrix of the scenery.

The received signal coming from the antenna located at $\bar{r}_R$ is amplified by a low noise amplifier (G_{LNA}) and then mixed with the signal coming from the slave generator; the signal produced has a conversion loss of α_{MIX} and is filtered by a pass-band filter (centred at 70 MHz). This Intermediate Frequency signal is in-phase and in-Quadrature demodulated at 70 MHz with the reference signal (LO_IQ, see fig. 1). Finally, the base band signals (I and Q) are passed through a digitally controlled amplifier (G_{AGC}) and digitally converted (A/D).

The DSP controls the gain and sampling of the intermediate frequency signal, the Phase-Looked-Loop (PLL) of the two signal generators, the sampling of I and Q, and the sequence of modulation. After four modulation periods, the DSP has acquired a complete set of holograms given by

$$H^{j,i}(\bar{r}_R, t) = k \cdot \text{rect}\left(\frac{t}{T_M}\right) \cdot$$

$$\cdot \int_{\bar{r}} \sqrt{G_T \ G_R} \ \frac{R^{j,i}(\bar{r})}{r^2} \cdot \quad (2.7)$$

$$\cdot \exp\left\{-j2\pi\left[\frac{1}{\lambda_0} + \frac{1}{2\Delta r} \text{stair}\left(\frac{t}{T_M}\right)\right]r_{RT}\right\} d\bar{r}$$

where $k = G_{LNA} \alpha_{MIX} G_{AGC} \lambda_0 \sqrt{\frac{P_T Z}{(4\pi)^3}}$ includes all the system parameters.

From eq. (2.6) the received signal is a phase-modulated signal and because the Step-Frequency modulation is slow compared with the instantaneous frequency, that is the time length of the step (T_M/N_M) is long compared with the period of the signal ($1/f$), the instantaneous frequency can be confused with the spectral frequency and eq. (2.7) can be written as

$$H^{j,i}(\bar{r}_R, f) = k \cdot \text{rect}\left(\frac{f}{B_{RF}}\right) \cdot$$

$$\cdot \int_{\bar{r}} \sqrt{G_T G_R} \ \frac{R^{j,i}(\bar{r})}{r^2} \cdot \quad (2.8)$$

$$\cdot \exp\left\{-j2\pi\left[\frac{1}{\lambda_0} + \frac{1}{2\Delta r} \text{stair}\left(\frac{f}{B_{RF}}\right)\right]r_{RT}\right\} d\bar{r}.$$

The acquired UHF holograms retain the amplitude and phase information of the interference between the transmitted wave and the received diffracted signal on the whole frequency bandwidth. It is important to note, from eqs. (2.8)

and (2.5), that the hologram phase

$$\Phi_H = 2\pi \left[\frac{1}{\lambda_0} + \frac{1}{2\Delta r} \text{ stair} \left(\frac{f}{B_{RF}} \right) \right] \cdot$$

$$\cdot \left[\sqrt{x - x_R - x_{TR})^2 + y^2 + (z - z_R)^2} + \quad (2.9) \right.$$

$$\left. + \sqrt{(x - x_R)^2 + y^2 + (z - z_R)^2} \right]$$

depends in a non-linear form on $\bar{r}_R = (x_R,\ 0,\ z_R)$: the location of the receiving antenna.

3. Wavefront reconstruction by means of Conjugate-Phase Matched imaging

In order to obtain the 3D image of the scenery observed, that is the acquired reflectivity function $\tilde{R}^{j,i}(r, \theta, \phi)$, a reconstruction process of the holography must be carried out. The *Conjugate-Phase Matched Method* is the optimal method (Mensa, 1991) and permits the image to be reconstructed without any aberration and degradation in the whole-investigated volume. The acquired holograms (2.8) are initially multiplied in space and frequency domains by two windows on the $(\bar{r}_R, f)$ axes ($\bar{r}_R$ describing the area (Σ) scanned with the radar, f the frequency in the band B_{RF}) and then they are match-filtered

$$\tilde{R}^{j,i}(\bar{r}) = \int_{\Sigma} \int_{B_{RF}} w_{\Sigma}(\bar{r}_R) \cdot w_{B_{RF}}(f) \cdot H^{j,i}(\bar{r}_R, f) \cdot$$

$$\cdot \exp \left\{ +j2\pi \cdot \left[\frac{1}{\lambda_0} + \frac{1}{2\Delta r} \cdot \text{stair} \left(\frac{f}{B_{RF}} \right) \right] \cdot r_{RT} \right\} \cdot$$

$$\cdot df \cdot d\bar{r}_R \cdot \qquad (3.1)$$

This method permits reconstruction of the optimal 3D image with the maximum resolution given from the size of the scanned area and from the radio frequency bandwidth.

Working in spherical co-ordinates, the reconstruction can be obtained by means of three integrals: one along the frequency axis, the other two along the axes of the scanned area.

The windowing of the hologram requires $N_T N_M$ real by complex multiplication, with N_T the number of locations of the antenna in the scanned area, and N_M the number of frequency steps; this means $2N_T N_M$ FLOPS (floating point operations). Supposing a look-up table has the values of the exponential function on the whole three dimensional investigated space, the holographic reconstruction requires $N_T N_M$ complex by complex multiplication for each voxel, that is $6N_T N_M$ FLOPS. Therefore, the overall computation power required (number of floating point operations per second per voxel) is

$$CP_V = \frac{1}{T_F} (8N_T N_M) \qquad (3.2)$$

where T_F is the computation time for each polarimetric image. In the case that T_F is set to 1 s, the throughput is about 0.16 MFLOPS per voxel.

4. Acquisition parameters

According to the theory outlined above, some care must be taken in designing the acquisition operations to obtain the desired resolution and to avoid the occurrence of unwanted phenomena such as aliasing. As regards resolution, the Synthetic Antenna length (the antenna side) and the range of frequency spanned needs to be decided. On the other hand, the aliasing is regulated by the frequency step (in a frequency stepped modulation) and by the spatial sampling, *i.e.* the spatial step used to build up the Synthetic Antenna (Soumekh, 1999).

Working on eq. (2.9), one can obtain two conditions for the resolution limits and two to avoid aliasing phenomena.

When a single frequency is used, it is not possible to have radial resolution in the far field (because the wavefront is planar). In the near field, thanks to the spherical front of the wave, it is possible to focus and radially localise the scattering centre. The antenna length needed to obtain the desired focusing of the object, can be obtained from the phase term in eq. (2.9) (Steinberg and Subbaram, 1991)
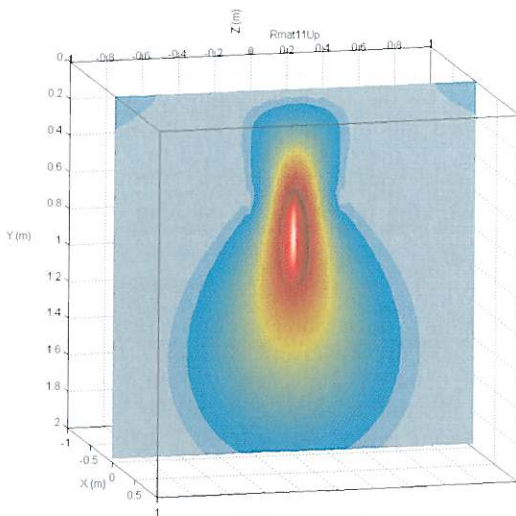
$$L = \frac{h}{\sqrt{\dfrac{\text{d. o. f.}}{7 \cdot \lambda}}} \qquad (4.1)$$
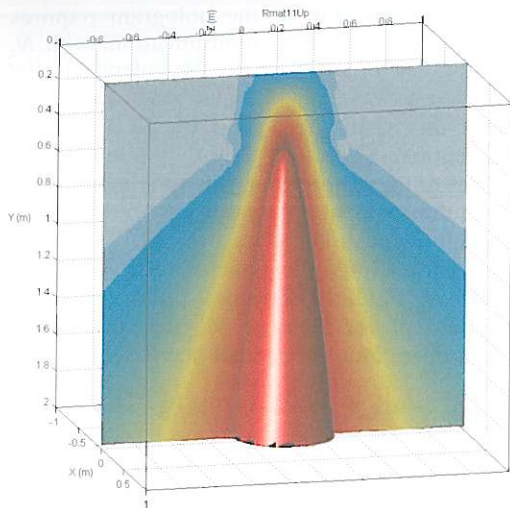
Fig. 2. Acquisition area 2×2 m^2. 3D rendering and slice. The lack of focus due to the restricted acquisition area is evident. The scattering point is 0.5 m deep.
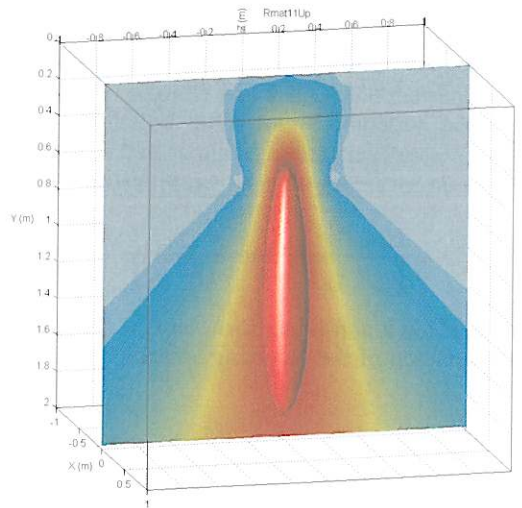
Fig. 3. Acquisition area 4×4 m^2. 3D rendering and slice. The lack of focus due to the restricted acquisition area is still clear even if reduced. The scattering point is 0.5 m deep.

Fig. 4. Frequency band 0.4-0.5 GHz; step 10 MHz. 3D rendering and slice. The low resolution due to a short frequency bandwidth is evident. The scattering centre is 0.5 m deep.
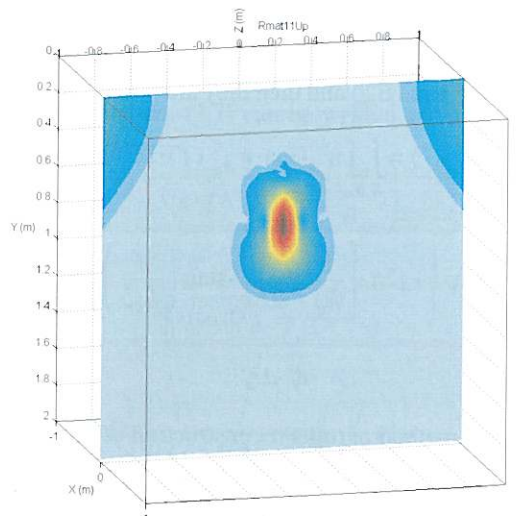
Fig. 5. Frequency band 0.4-0.7 GHz; step 10 MHz. Slice of the 3D rendering. The higher resolution due to the wider frequency bandwidth is evident. The scattering centre is 0.5 m deep.

where d.o.f. is the depth of focus (length of the focused zone); L is the minimum effective dimension of the scanned area (minimum synthetic aperture antenna dimension); h is the depth of the scattering point; λ is the wavelength in the medium (m).

If the scanned area is not large enough in terms of wavelengths, lack of focus appears so that nearby scattering centres could even be merged together (see figs. 2 and 3).

As far as the bandwidth needed to obtain the desired resolution is concerned, it can be evaluated, again from eq. (2.9), in the far field, using the following formula:

$$B_{RF} = c / (\sqrt{\varepsilon_r} \cdot 2 \cdot \Delta r) \qquad (4.2)$$

where c = light velocity in vacuum ($3 \ 10^8$ m/s); ε_r = relative dielectric permittivity of the medium.

Using the same B_{RF} and considering scattering centres located in the near field of the synthetic aperture, the radial resolution property is enhanced. This is due to the non-linear phase of the back-scattered wavefront in the scanned area, that is the Fresnel diffraction pattern. A wrong choice of the bandwidth leads to a poor definition of the scattering object (see figs. 4 and 5).

Given the size of the volume to be investigated, the maximum radial distance is known. In order to avoid the frequency aliasing condition, the following formula can be drawn from eq. (2.9):

$$\Delta f < \frac{c}{\sqrt{\varepsilon_r} \cdot 4 \cdot r_{max}} \qquad (4.3)$$

where r_{max} is the maximum radial distance to be scanned.

If this condition is not fulfilled, artefacts will appear in the reconstructed image (see fig. 6).

The building up of a Synthetic Aperture Antenna involves moving the dipole step by step along a regular grid on the ground. The condition that must be fulfilled by this step to avoid spatial aliasing effects can again be obtained from eq. (2.9) and written according to the following formula:

$$\Delta x \leq \frac{\lambda}{4} \qquad (4.4)$$
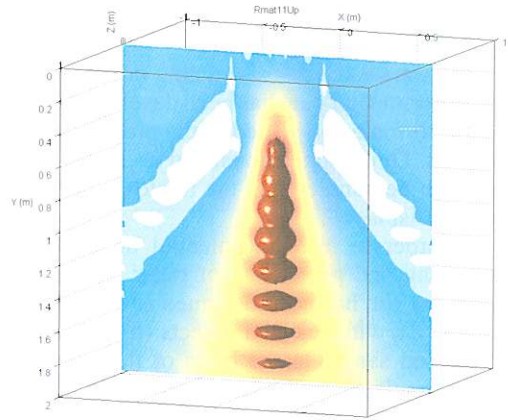
Fig. 6. Frequency aliasing effect. 3D rendering and slice. The ghosts of the object along the vertical axis under the scattering point are evident. The scattering centre is 0.5 m deep.
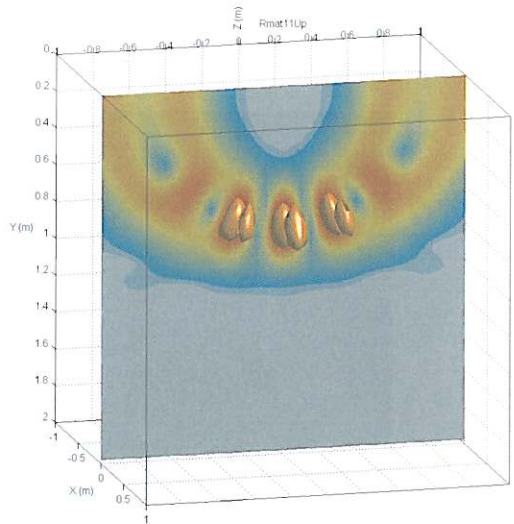
Fig. 7. Spatial aliasing effect. 3D rendering and slice. The ghosts of the object on a spherical surface containing the scattering point are evident The scattering centre is 0.5 m deep.

where λ is the wavelength in the medium; Δx is the sampling step of the scanned area.

If this condition is not fulfilled, artefacts will appear in the reconstructed image (see fig. 7).

5. Simulation results

Software either for simulating or for analysing experimental data has been developed based on the formulas presented in the preceding paragraphs. Three-dimensional and bi-dimensional data can be handled and the related renderings can be displayed.

In order to test the potential of hologram collecting and processing of radar data, a full scale test site has been designed and constructed (fig. 8), with selected objects (fig. 9) buried in classed sand. On the basis of this test site, some simulations have been carried out obtaining: three-dimensional renderings; two-dimensional renderings; conventional radar images.

Three-dimensional images are a more realistic representation of the buried scattering objects. The presented images refer to synthetic reconstruction of data, as they were collected on the test site, in dry (figs. 10 and 11) and wet
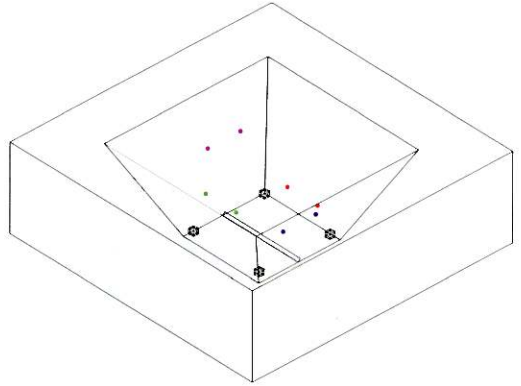
Fig. 8. Sketch of the test site. Red points represent the two lower spheres (0.5 m from the bottom; blue points represent two spheres at 1.0 m from the bottom; green points represent two spheres at 1.5 m from the bottom; pink points represent two spheres at 2.0 m from the bottom. The *L*-shaped aluminium bar and the corner reflectors are also drawn.
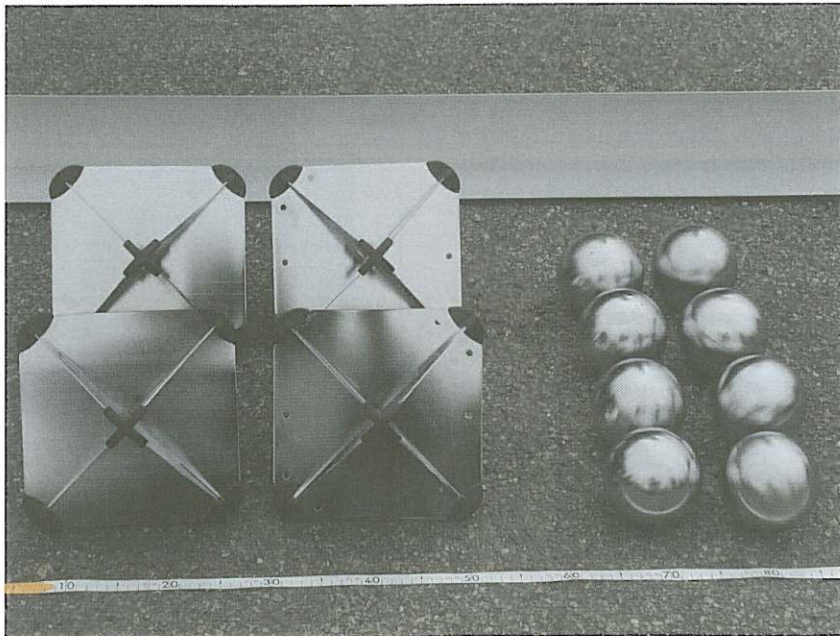
Fig. 9. The buried objects: 8 spheres (diameter = 0.08 m); 4 corner reflectors (longest size = 0.28 m); 1 *L*-shaped corner bar (length = 2.5 m, *L* size = 0.1 m).
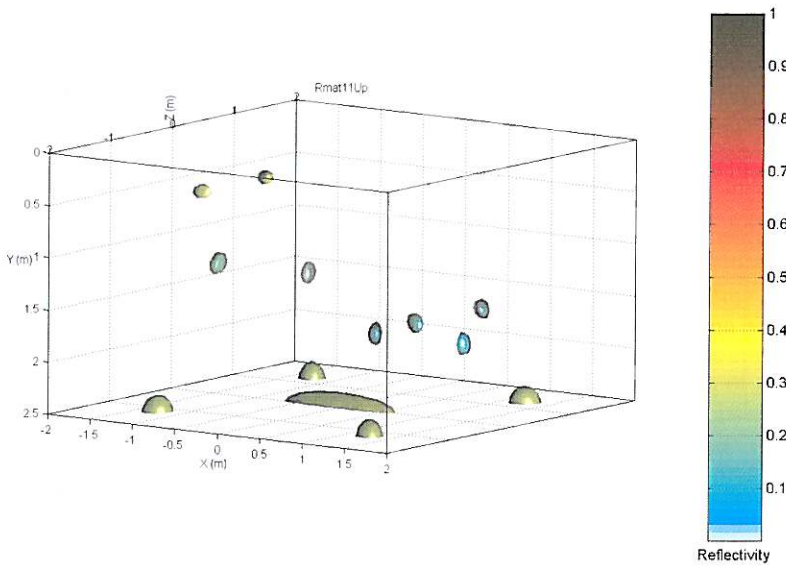
Fig. 10. Rendering with dry sand conditions; polarisation HH ($\sigma = 10^{-5}$; $\varepsilon = 4$). Scattering centres are evident together with the aluminium bar.
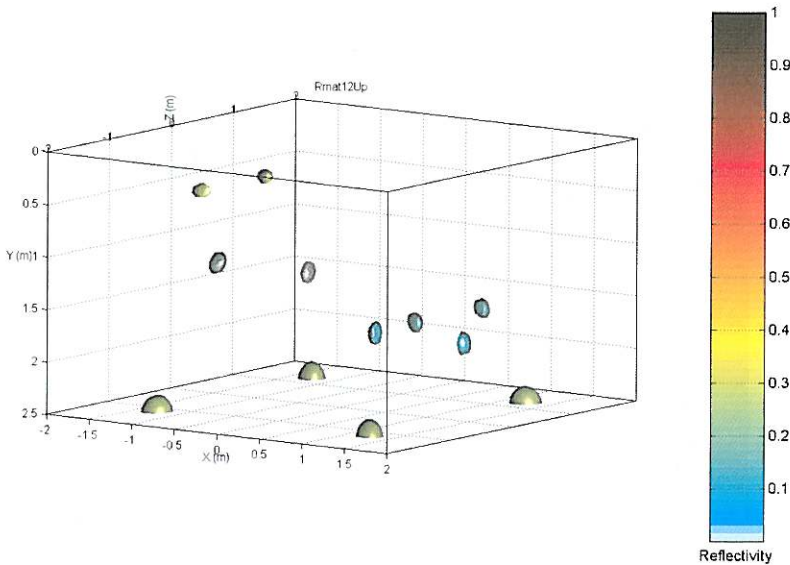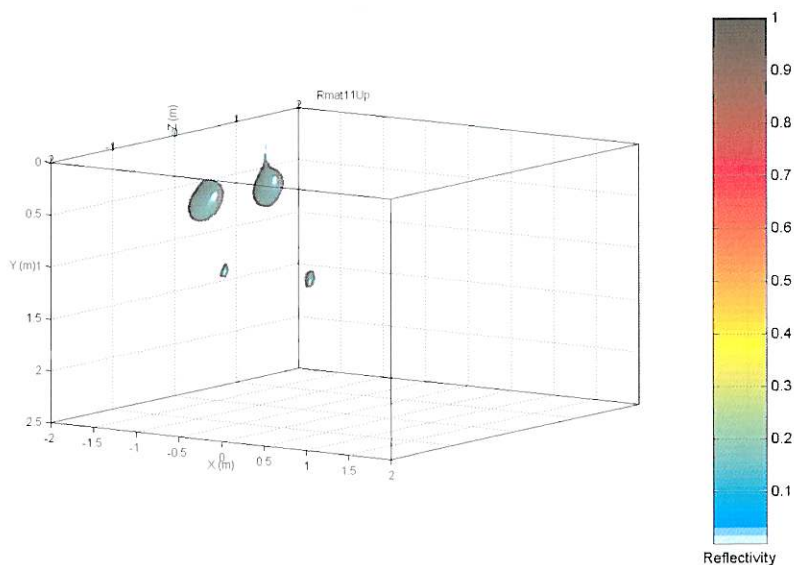

Fig. 11. Rendering with dry sand conditions polarisation HV ($\sigma = 10^{-5}$; $\varepsilon = 4$). The aluminium bar is no longer visible in as much as the reflected signal, polarised by the corner of the bar, is orthogonal with respect to the receiving antenna.

1115

Fig. 12. Rendering with wet sand conditions; polarisation HH ($\sigma = 10^{-2}$; $\varepsilon = 4$). The attenuation due to the high conductivity does not allow to detect targets deeper than 1 m.
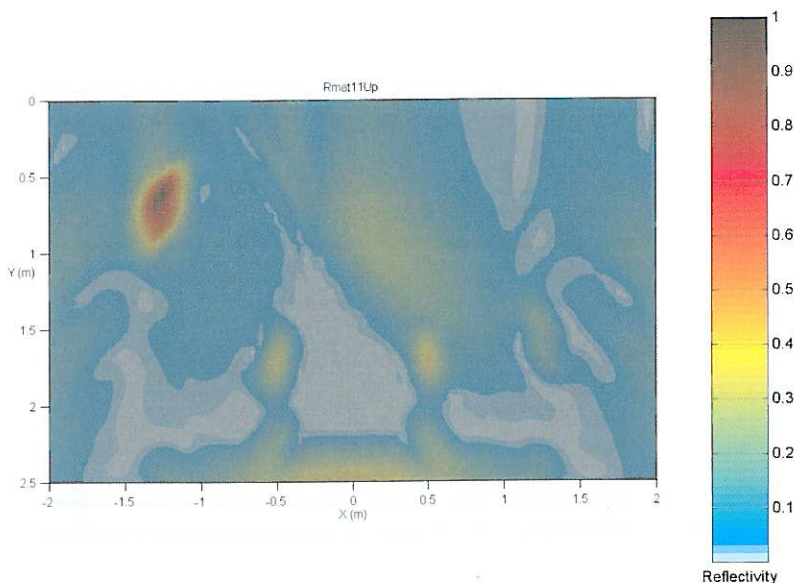
Fig. 13. 2D holographic reconstruction. Even if it is a 2D reconstruction, the better readability of results is evident.
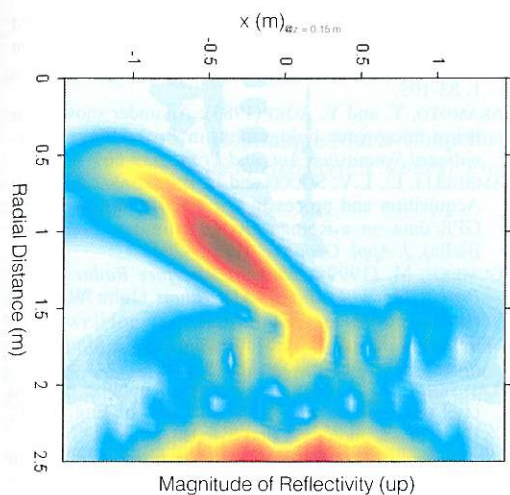
Fig. 14. Reconstruction in the conventional radar image from holographic data. The hyperbola on the top left of the image refers to the same object (a sphere) represented as a circle in fig. 13.

(fig. 12) conditions. The attenuation effect in wet conditions is evident avoiding the possibility to detect the deepest targets. The bi-dimensional holographic images show the lateral effects deriving from the shape of the emitting and receiving radiation patterns of the antennas (fig. 13): lateral objects are attributed to the vertical section of the ground underlying the profile.

From the data collected in the SAR it is also possible to reconstruct the radar section as if it were collected in the conventional near zero-offset way (fig. 14). By reconstructing the radar data in this way hyperbolic artefacts appear as commonly seen in conventional radar around the top of a scattering object.

6. Discussion and conclusions

In studying the possibility of realising a Holographic Ground Probing Radar, advantages and disadvantages have been considered even if some of the latter can be attributed to the early stage of the study and to a lack of optimisation. The main advantages can be summarised as follows: higher signal to noise ratio on the radar image is obtained thanks to the higher energy radiated in long modulations periods; more complete recovery of the information carried by the wavefield due to the use of phase recovery and of the four polarisation acquisitions; less distortion in the images, that are much freer from hyperbolic artefacts, due to holographic acquisition and processing.

On the other hand, the main disadvantages, at least at this stage, can be summarised as follows: more acquisition time and the need for a higher precision in antenna positioning due to the resolution and anti-alias conditions outlined in the preceding paragraph of this paper; more processing time due to the heavy integrals, that are performed in a straightforward manner and with routines which are not optimised.

As far as further developments are concerned, an automatic set up for the movement and position of antennas is under design. A set of routines to speed up, as far as possible, with minimum precision loss, to reduce processing time is also under development.

Acknowledgements

REFERENCES

AL-GHAMDI, A.G. and M.S. AFIFI (1996): Near range resolution and object detection in high interference environment, in *Proceedings GPR '96, Sandai, Japan*, 399-403.

BAE, S.H., H.S. KIM and W.S. YOON (1996): Case studies of the application of Ground Penetrating Radar Technology in detection of underground utilities and structures safety diagnosis, in *Proceedings GPR '96, Sandai, Japan*, 467-472.

DANIELS, D.J., D.J. GUNTON and H.F. SCOTT (Editors) (1988): Special Issue on Subsurface Radar, *Proc. Inst. Electr. Eng.*, **135** (F, 4).

DANIELS, J.J., R. ROBERTS and M. VENDL (1992): Site studies of Ground Penetrating Radar for monitoring petroleum product contaminats, in *Proceedings of SAGEEP*, 597-608.

DAVIS, J.L. and A.P. ANNAN (1989): Ground Penetrating Radar for High-Resolution mapping of soil and rock stratigraphy, *Geophys. Prospect.*, **37**, 531-551.

GIUBBOLINI, L. (1999): A microwave imaging radar in the near field for anticollision (MIRANDA), *IEEE Trans. Microwave Theory Tech.*, **47** (9).

GOODMAN, D. (1994): Ground-penetrating radar simulation in engineering and archaelogy, *Geophysics*, **59** (2), 224-232.

GUO, T.J., A. GODIO, L. SAMBUELLI and G. RANIERI (1997): Experiments for the detection of hydrocarbon contamination using Ground Penetrating Radar, in *International Symposium «Engineering and Environmental Geophysics» Chengdu, P.R. China, October 25-30*, 450-457.

LEUSCHEN, C., N. GOODMAN, C. ALLEN and R. PLUMB (1996): An interferometric technique for synthetic-aperture Ground Penetrating Radar, in *Proceedings GPR '96, Sandai, Japan*, 405-409.

MENSA, D.L. (1991): *High Resolution Radar Cross-Section Imaging* (Artech House), 139-198.

MIWA, T., M. SATO and H. NIITSUMA (1996): Measurement and characterisation of subsurface fracture by polarimetric borehole radar, in *Proceedings GPR '96, Sandai, Japan*, 377-381.

PIPAN, M., I. FINETTI and F. FERIGO (1996): Multi-fold GPR techniques with applications to high-resolution studies: two case histories, *Eur. J. Env. Eng. Geophys.*, 1, 83-103.

SAKAMOTO, Y. and Y. AOKI (1985): An under snow radar using microwave holography, in *Proceedings International Symposium Ant. and Prop.*, 659-661.

SAMBUELLI, L., L.V. SOCCO and L. BRECCIAROLI (1998): Acquisition and processing of electric, magnetic and GPR data on a Roman site (Victimulae, Salussola, Biella), *J. Appl. Geophys.*, **41**, 189-204.

SOUMEKH, M. (1999): *Synthetic Aperture Radar Signal Processing with Matlab Algorithms* (John Wiley & Sons), 397-418.

STEINBERG, B.D. and H.M. SUBBARAM (1991): *Microwave Imaging Technique* (John Wiley & Sons, Inc), 34-38.

ULRIKSEN, C.P.F. (1982): Application of impulse radar to civil engineering, *Ph.D. Thesis*, Dept. of Eng. Geol., Univ. of Technology, Lund Sweden, pp. 175.

VAN DEEN, J.K. (1996): 3D ground probing radar, in *Proceedings GPR '96, Sandai, Japan*, 295-298.

YAMAGUCHI, Y., H. KASAHARA, T. MORIYAMA and H. YAMADA (1996): Polarimetric detection of objects by a deep sounding FM-CW radar, in *Proceedings GPR '96, Sandai, Japan*, 373-376.